# Geophysical Research Letters

**Key Points:**
- Convection occurs in 1%–5% of precipitating regions of extratropical cyclones over eastern United States and contributes 1%–15% of total precipitation
- The majority of upright convection occurs ahead of the cold front and disperses into other regions as the cyclone ages
- While convection produces larger rain rates, cyclones with greater total precipitation do not have a large convective contribution

## Upright Convection in Extratropical Cyclones: A Survey Using Ground-Based Radar Data Over the United States

Jeyavinoth Jeyaratnam[1,2] , James F. Booth[1,2,3] , Catherine M. Naud[3,4] ,
Z. Johnny Luo[1,2] , and Cameron R. Homeyer[5]

[1]Earth and Environmental Sciences Department, Graduate Center, The City University of New York, New York, NY, USA, [2]Department of Earth and Atmospheric Sciences, The City College of New York, The City University of New York, New York, NY, USA, [3]NASA Goddard Institute of Space Studies, New York, NY, USA, [4]Applied Physics and Applied Mathematics Department, Columbia University of New York, New York, New York, USA, [5]School of Meteorology, University of Oklahoma, Norman, OK, USA

**Abstract** Upright convection can impact extratropical cyclone (ETC) precipitation and dynamics differently than isentropic ascent, but how often it occurs and how much it contributes to total precipitation within an ETC have not been systematically documented in previous literature. Herein, convection in ETCs is analyzed using ground-based radar observations over the Eastern United States. Convection occupies 1%–5% of the precipitating region and constitutes 1%–15% of total cyclone precipitation. Furthermore, the location of convective activity occurs preferentially in the warm sector early in a cyclone's life cycle, and then as the storm evolves, more convection occurs along and behind the cold front. The precipitation rates in regions with convection are more likely to be stronger than those in other precipitating regions of the cyclone. However, the cyclones with the largest area-average precipitation rates include only a small contribution from convection.

**Plain Language Summary** This research is motivated by the potential influence of convection on extratropical cyclone circulation. We utilize a newly derived dataset of upright convection and a cyclone-tracking framework to quantify convective activity in extratropical cyclones over the United States, east of the Rocky Mountains. We find that upright convection only occupies a small portion of the precipitating region, and the relative contribution to total precipitation has relatively small variability as the cyclone evolves. We find that the location of convective activity occurs preferentially in the warm sector early in a cyclone's life cycle, and as the storm evolves, more convection occurs along and behind the cold front. We find that precipitation rates in regions with convection are more likely to be stronger than those in other precipitating regions of the cyclone. However, the cyclones with the largest area-average precipitation rates include only a small contribution from convection.

## 1. Introduction

The majority of midlatitude precipitation is generated by extratropical cyclones (ETCs; Hawcroft et al., 2012), as are the extremes (Pfahl & Wernli, 2012), which makes it critical that we understand and properly model ETC precipitation formation. The key components involved in ETC precipitation formation are moisture convergence, vertical lifting, and microphysical processes that convert water to falling condensate. This paper focuses on the vertical lifting component, specifically the role of upright convection within ETCs.

Understanding upright convection in ETCs is important for multiple reasons: (a) microphysics within convection can differ from that in isentropic ascent-impacting ETC rain rates; (b) there are differences in the vertical profile of diabatic heating associated with different lifting processes (e.g., Houze, 2014, Chapter 6; and see Homeyer et al., 2014 for an example in the extratropics), and these affect ETC winds (reviewed in Colle et al., 2015); and (c) in general circulation models (GCMs), parameterized convection includes microphysics assumptions, which ties back into (a), and vertical mass flux and entrainment, which ties back into (b). The parameterizations continue to be a major focus in model development, and there is a need for benchmarks of midlatitude convective activity for comparison (Booth, Naud, & Willison, 2018).

In numerical weather prediction (NWP), ETCs can have different vertical profiles of latent heating for isentropic lifting or upright convection, which affects the growth rate of ETCs (Tierney et al., 2018) and the

moisture flux within the modeled warm conveyor belt (WCB; Boutle et al., 2011). Related to this, explosive ETCs in NWP models are known to be sensitive to the choice of the parameterized convection scheme (e.g., Reed et al., 1993). Thus, understanding convection within ETCs could have implications for understanding cyclone intensification.

The work herein is also motivated by a recent study showing that GCMs and NWP models, including those used to create reanalysis products, have a wide range of contributions from their convection parameterizations to ETC precipitation (Booth, Naud, & Willison, 2018). Also, the microphysics within parameterized convection schemes differs from that of the large-scale microphysics scheme (e.g., Elsaesser et al., 2017; Zhao et al., 2018) and this impacts the modeled rain rates (Hawcroft et al., 2017), clouds, and possibly the relative humidity distribution within ETCs (Catto et al., 2010). Therefore, it is important to characterize the behavior of upright convection within ETCs in observations so that we can properly assess the behavior of convective parameterizations.

Previous results have focused on convection within oceanic ETCs using case studies (Crespo & Posselt, 2016; Flaounas et al., 2016 and Oertel et al., 2019). Oertel et al. (2019) analyzed one oceanic cyclone in which convection occurs frequently and consistently in the warm sector. The convection they identified had weak updraft vertical velocities; however, the regions with active convection produced intense surface precipitation. Here instead, we consider a relatively large sample of ETCs over the United States, east of the Rocky Mountains. For this region, previous work has analyzed convection along the cold front (Hobbs, 1978; Houze et al., 1976) and mesoscale convective systems (Feng et al., 2018). Agel et al. (2019) found the potential for convective activity to be very important to extreme precipitation events in the Northeast United States. However, to our knowledge, no previous study has calculated the cyclone-averaged contribution of convective precipitation to total precipitation produced by ETCs.

Using a set of 115 cyclone tracks over the contiguous United States (CONUS), we analyze upright convection that has been identified using signatures in ground-based Next Generation Weather Radar (NEXRAD) data (Starzec et al., 2017). The results presented herein report on (a) the extent of convection and its contribution in terms of total precipitation throughout the life cycle of an ETC over the CONUS, (b) the preferred location of identified convection with respect to its lifecycle, and (c) the relationship between the contribution of convective precipitation, precipitation rates, and total precipitation of cyclones.

## 2. Data and Methods

This research utilizes reanalysis products and ground-based radar data. ETCs and their fronts are identified using reanalysis. Then, precipitation around the cyclones is analyzed and sorted based on convection identified from ground-based radar observations.

The precipitation dataset used is the National Centers for Environmental Prediction Stage IV data, which is a mosaic of regional hourly multi-sensor (radar and gauges) precipitation analysis produced by National Weather Service River Forecast Centers over CONUS (Lin & Mitchell, 2005) on a 4-km grid (Baldwin & Mitchell, 1998).

The reanalysis used is the Modern-Era Retrospective Analysis for Research and Applications, Version 2 (MERRA-2; Gelaro et al., 2017). Sea-level pressure (SLP), temperature (T), wind-speeds (U and V), and specific humidity (Q) at 850 hPa are extracted for each 6-hour time step from hourly files (i.e., the MERRA-2 tavg1_2d_slv files; GMAO, 2015). MERRA-2 data is available on a 0.5° latitude by 0.625° longitude global grid.

Lagrangian tracks for the ETCs are identified using the Modeling, Analysis and Prediction Climatology of Midlatitude Storminess (MCMS) algorithm (Bauer et al., 2016). MCMS is applied to 6-hourly SLP data from reanalysis. The algorithm is described in detail in Bauer et al. (2016), so we provide only a brief overview here. First, local minima in SLP are used to identify low-pressure centers. These centers are then filtered using a SLP threshold dependent on hemisphere, season, and topography. Next, the low-pressure centers are linked in time to create tracks with 6-hour increments. For this paper, each 6-hour instance is referred to as a *cyclone* and the entire time-linked set of cyclones are referred to as a *track*.

In this study, cyclone center latitude and longitude are retained for tracks with a minimum duration of 30 hours and minimum travel distance of 1,000 km. ETCs are tracked from 2014 to 2016 because this coincided with the timing of the availability of the ground-based convection data detailed below. From the full set of ETC tracks, 115 tracks that have precipitation over the United States east of the Rocky Mountains are selected (within a bounding box from 22°N to 46°N and 103°W to 61°W). We confirmed that there is nothing unique about the intensification rates (defined as 6-hourly dSLP/dt) or paths of these 115 tracks by comparing the intensification rate distributions and track location density to a larger set of tracks in the same region for the time period from 1979–2013 (around 1,341 tracks).

For each 6-hourly cyclone center location, we use the nearest hour of Stage IV precipitation data and retain values within 1,000 km from the center. For each cyclone, we compute area-average precipitation ($PR_{AA}$), which we define as the sum of total precipitation within 1,000 km of the cyclone center divided by the area (see Text S1 from the Supporting Information for equations defining our metrics). Later, we group cyclones relative to their time step of maximum $PR_{AA}$.

The study region selected contains a dense network of NEXRAD radars, which obtain volumes of clouds and precipitation at approximately 5-minute intervals. Composites of radar reflectivity from these three-dimensional NEXRAD observations on a regular 0.02° longitude-latitude grid with 1-km vertical resolution, known as GridRad data (http://gridrad.org; Homeyer & Bowman, 2017), are created every 5 minutes within the Stage IV hour matched with each 6-hour ETC location and used to identify convection. For use in this study, convection identifications consist of the combination of the convection and convective updraft classifications from the Starzec et al. (2017) algorithm. A summary of the classification is in Supporting Information, full details are in Starzec et al. (2017). We apply a land mask to the cyclones before performing any analysis. This is due to the merged land-based radar datasets potentially having biases due to lack of overlapping and near-surface radar data.

We are interested in quantifying convective activity in ETCs at different life stages from observations. To do this, convection identified from GridRad is re-gridded to Stage IV resolution (4 km) by counting the number of radar-identified convective pixels that occupy each 4-km grid cell. To study convection with respect to ETC life cycle, the time steps for each track are indexed relative to the time step with maximum $PR_{AA}$, as in Booth, Naud, and Willison (2018). The time step with maximum $PR_{AA}$ is indexed as time zero ($t = 0$), with future time steps having positive incremental indices and time steps before maximum $PR_{AA}$ (per cyclone) having negative indices.

For our analysis, we compute the following metrics (mathematical representations of the metrics are provided in the Supporting Information):

1. *Subgrid convective extent*—the ratio of the count of convection to the total number of points from GridRad's 0.02° grid that fall into the 4-km Stage IV grid cell, that is, this is a fraction per Stage IV grid cell.
2. *Cyclone convective extent*—the ratio of cyclone area flagged with convection to the total area in which precipitation occurs, that is, the subgrid convective extent averaged over the entire cyclone precipitation region.
3. *Convective precipitation rate*—the product of the subgrid convective extent and the stage IV precipitation rate per grid cell.
4. *Cyclone convective precipitation rate*—convective precipitation rates averaged over the entire cyclone precipitation region
5. *Convective contribution*—the sum of convective precipitation rates divided by the sum of total precipitation rates, that is, the fraction of contribution from convection to the total precipitation.

Note that for cyclone averages in the metrics above, averages do not include points at which the rain rate is zero. This differs from $PR_{AA}$, in which the average uses all points within 1000 km of cyclone center even those with a rain rate of zero. $PR_{AA}$ has to be defined this way, that is, using a fixed size for the averaging region, so that we can sort the cyclone into a precipitation life cycle. However, we also define a conditional precipitation rate: $PR_{RR}$; the precipitation rate averaged within a 1,000-km radius of the cyclone excluding zero values.
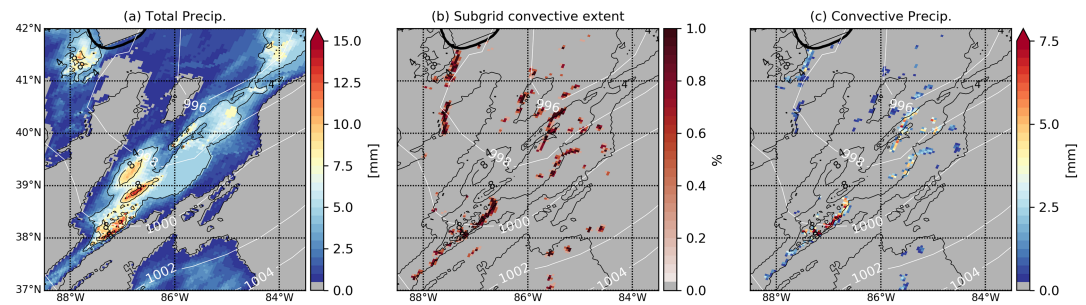
**Figure 1.** (a) Total precipitation, (b) subgrid convective extent, and (c) the partial-grid convective precipitation for the time step with the maximum total precipitation for a sample tracked extratropical cyclone on March 24, 2016. The white contours show the sea-level pressure and the black contours show the total precipitation.

We also analyze the location of convection relative to the surface temperature fronts. For this study, cold fronts are detected using a combination of an abrupt change in the potential temperature field (Hewson, 1998) and temporal changes in meridional winds at 850 hPa (Simmonds et al., 2012). Naud et al. (2016) contains the detailed methodology to identify fronts. Here, we provide a brief overview. Hewson (1998) uses a zero along vector divergence of the potential temperature gradient to identify fronts. The sign of the geostrophic thermal advection is then used to distinguish cold fronts (negative) from warm fronts (positive; Hewson, 1998; Naud et al., 2010). Warm fronts are detected using the Hewson (1998) method, at 1 km above the surface. In strong baroclinic environments, Hewson (1998) is successful in detecting fronts, while in a weak baroclinic environment, Simmonds et al. (2012) perform better for cold fronts. Their method uses the change in meridional winds from the northwest quadrant to the southwest quadrant above a magnitude of 2 ms$^{-1}$ to locate cold fronts.

## 3. Results

To introduce our metrics for quantifying convection on the Stage IV grid, we begin with a typical case of an ETC selected from our set of 115 tracks. For this ETC, Figure 1 shows precipitation and convective activity at the time in the cyclone life cycle when the maximum PR$_{AA}$ occurred. The region shown is south/southwest of the cyclone center, as indicated by the SLP contours (white lines). Figure 1a shows Stage IV total precipitation (mm/hr) on its native 4-km resolution grid. Figure 1b shows the subgrid convective extent per grid cell obtained from counting convection flagged by radar that fall into the Stage IV grid cell. This is the first result from our analysis: the flagged convective activity is found across the entire precipitation region of the cyclone, and occurs in a disperse patchwork of locations, rather than in a contiguous region.

In the Stage IV grid, 4% of the precipitating grid cells (within 1,000 km of the cyclone center) are flagged as convective (Figure 1b). In the majority of these convection-flagged grid cells (64%), the subgrid convective extent is at least 50% per grid cell. Figure 1c shows the partial-grid convective precipitation, which is the product of the information from Figure 1a,b. This metric shows that regions of convective activity are not confined to areas with strong precipitation rates.

Using the same methodology from the case study shown in Figure 1, we analyze 115 ETCs' tracks. Due to lack of radar data in some cases, the total number of individual snapshots we have is 642. This means we do not have 115 cyclones at every point of the life cycle. Figure 2a shows the life cycle of an ETC for 6 hours prior and after total maximum precipitation (PR$_{AA}$) for the same case as shown in Figure 1. The detected cyclone fronts (red and blue lines) for each time step are shown along with total precipitation (Figure 2a). The majority of the precipitation is situated within the warm sector of the cyclone (until late in the storm's life cycle), south of the warm front and east of the cold front. This is the region with the most active convection reported in case studies over the ocean (Crespo & Posselt, 2016 and Oertel et al., 2019). Figure 2b shows cyclone convective extent (solid black line) and convective contribution (dotted black line) averaged at every 6-hour time step of the life cycle of an ETC (relative to maximum PR$_{AA}$). The cyclone convective extent varies from 1%–5% and the convective contribution varies from 1%–15% (Figure 2b). The figure shows that
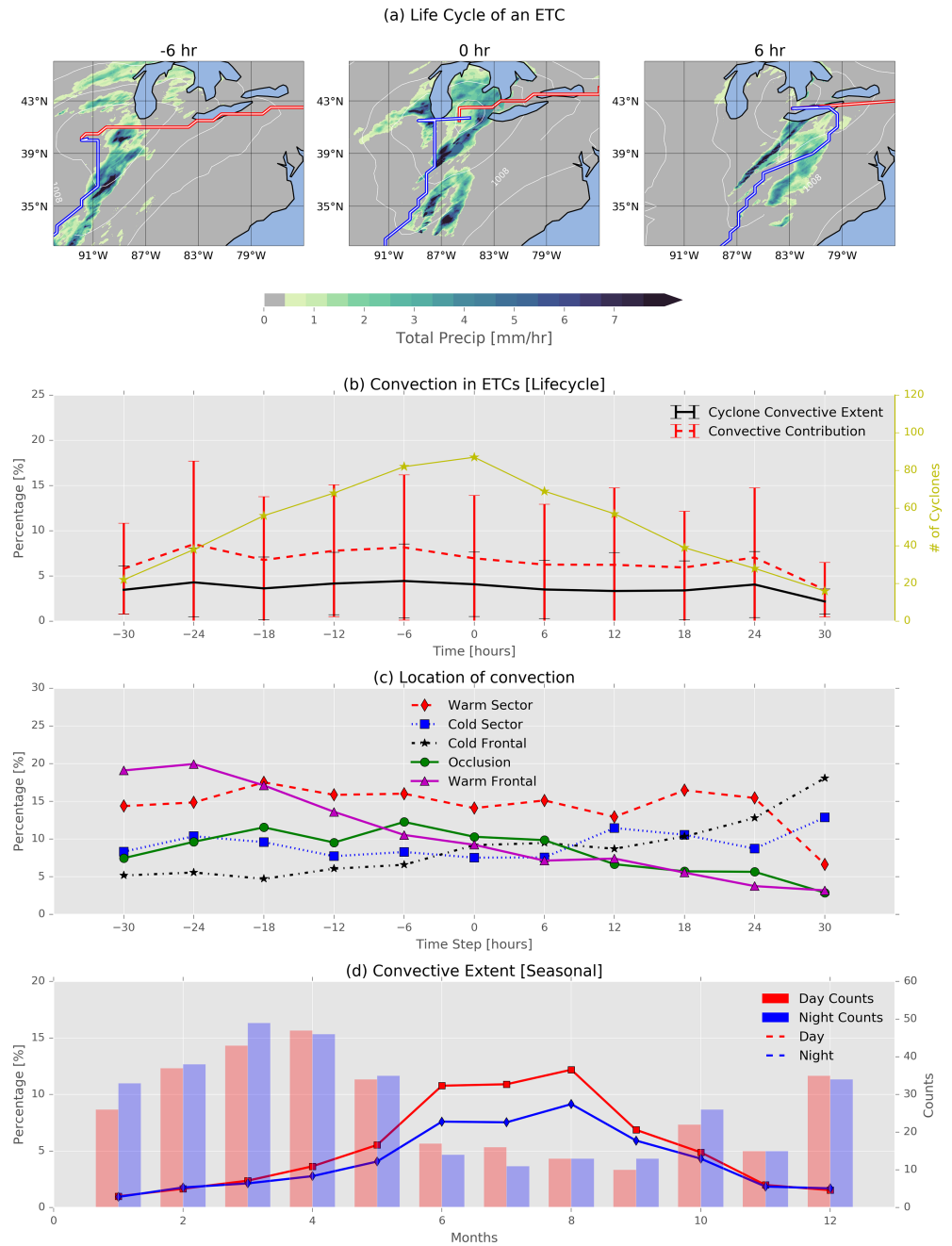
**Figure 2.** (a) Shows three 6-hourly time steps of a sample extratropical cyclone (ETC; same as shown in Figure 1), with 0 being the time step with the total maximum area-average precipitation ($PR_{AA}$). White lines with blue border show the detected cold fronts, and white lines with red border show the warm fronts. The white contour lines show the sea-level pressure which is overlaid on top of the total precipitation for the given time step of an ETC on a MERRA-2 grid. (b) shows the cyclone convective extent (black) and the convective contribution (dotted red line) for the life cycle of an ETC. Time index 0 is the time step of maximum $PR_{AA}$. Yellow line shows the number of cyclones included in the analysis for each time step. (c) shows the mean percentage of convection in different sectors of an extratropical cyclone sorted by 6-hourly time steps. Time index 0 is the time step of maximum $PR_{AA}$. Red line denotes the percentage of convection in the warm sector (east and equatorward of the fronts), blue denotes the cold sector (west and equatorward), green denotes the occlusion region (west and poleward), and purple denotes the warm frontal region (along and poleward of the warm front). Black denotes the cold frontal region (100 km width). (d) shows the diurnal variation of cyclone convective extent sorted by months. Red shows the day time values, whereas blue shows the night time values. The lines show the cyclone convective extent and the bars show the counts of cyclones per month.
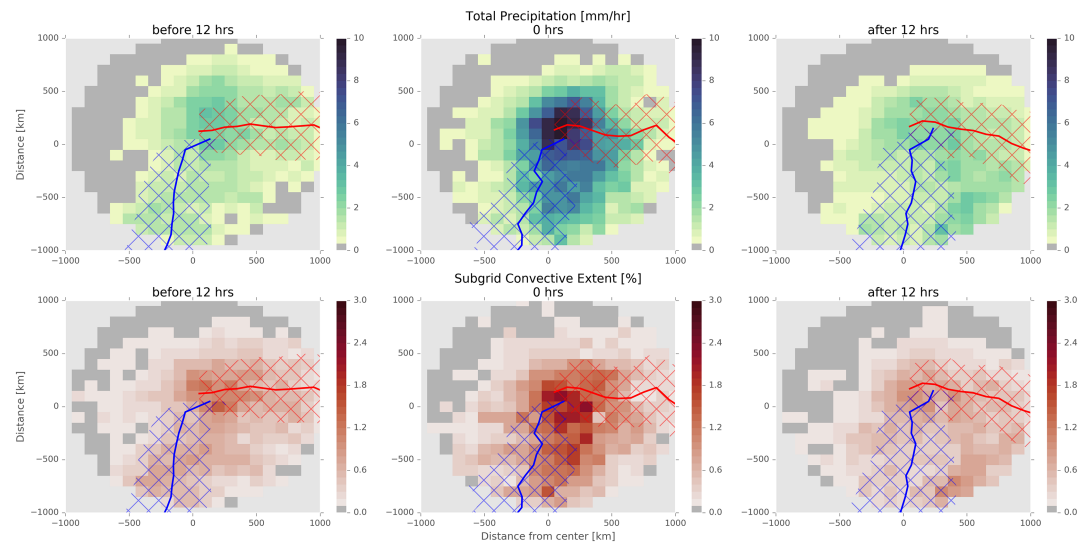
**Figure 3.** Top row shows the total precipitation of cyclone averages, at times relative to the cyclone-averaged precipitation maximum. Bottom row shows the average subgrid convective extent. The blue lines show the average cold front from all the cyclones, and the red line shows the average warm front from all the cyclones. The hashes show the extent of identifies fronts over all the extratropical cyclones within the specified time period.

cyclone convective extent and convective fraction do not vary much through the life cycle of an ETC. This is not to say that the preferred location of convection does not vary with time.

Next, we divide the spatial footprint of each of the 642 cyclones into five sections to identify the preferred location of convection: (a) eastward of the cold front and equatorward of the warm front (i.e., the *warm sector*), (b) along and poleward of the warm front (*warm frontal*), (c) westward of the cold front and equator-ward of the warm front (*cold sector*), (d) westward of the cold front and pole-ward of the warm front (*occlusion*), and (e) along the cold front, defined as $\pm 50$ km from the detected fronts (*cold frontal*). Figure 2c shows the percent of convection in each region, sorted by the life-cycle for all 642 cyclones. During the early stages of the ETC, ~35% of the convection is in the warm sector and warm frontal regions (sum of red and purple lines, respectively). As the cyclone ages, the percentage of convection in the warm sector (~15%) remains the same while the amount of convection in the warm frontal regions drops to ~5%. After the time step with maximum $PR_{AA}$, the percentage of convection shifts from warm frontal to along and behind the cold front (cold sector). Thus, there is a shift in convective activity from the warm sector to the cold frontal region and cold sector during the life cycle of the ETCs.

In addition, we analyze seasonal and diurnal cycle differences in convective extent (Figure 2d). During the summer months, we have the most convective extent (~15%), and during the winter months, it is low at about ~2%. Cyclones during the day have higher convective extent than at night. This difference is exaggerated during the summer months. All three of these results are consistent with the thermodynamic response of the strong diurnal cycle of land surface temperatures during summer. The results also agree with Agel et al. (2019), their summer time cluster had the largest potential for convection.

To examine the most probable spatial location of convective activity, we created cyclone-centered composites. Figure 3 shows the cyclone composite mean of total precipitation (top row) and the subgrid convective extent (bottom row) at different life stages of the ETCs: all time steps prior to 12 hours with maximum $PR_{AA}$, at maximum $PR_{AA}$, and time steps past 12 hours with maximum $PR_{AA}$. The composites suggest that the subgrid convective extent is largest at the time of maximum $PR_{AA}$; however, its relative contribution does not increase (Figure 2b). Additionally, this figure shows the mean location of the identified cold fronts (blue) and warm fronts (red) for the different time steps of the ETC. Prior to 12 hours, convection is predominantly identified near the warm front or warm frontal regions and it shifts towards the cold frontal regions during the later stages of the ETC (confirming our statistics shown in Figure 2c).
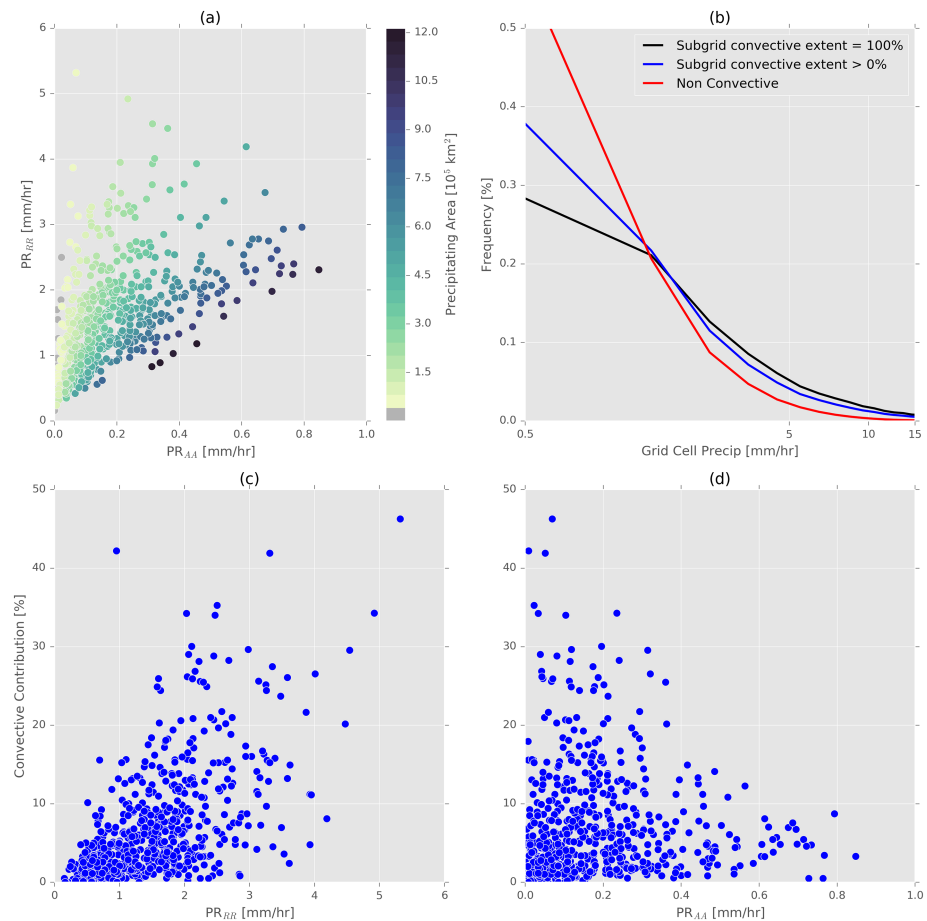
**Figure 4.** (a) Area-averaged precipitation rate ($PR_{AA}$) versus conditional precipitation rate ($PR_{RR}$), with color shading showing the number of raining cells within 1,000 km of the cyclone center. (b) Frequency of Stage IV precipitating grid cells separated by grid cells with no convection (red), subgrid convective extent >0 (blue), and 100% subgrid convective extent (black). (c) Conditional precipitation rate ($PR_{RR}$) vs convective contribution. (d) Area-averaged precipitation ($PR_{AA}$) versus convective contribution.

We next explore the relationship between precipitation rates (cyclone-averaged and total) and convective activity. To add aid in the interpretation of the influence of convection, we first analyze the relationship between the area-averaged precipitation rate ($PR_{AA}$), the conditional precipitation rate ($PR_{RR}$), and the number of precipitating cells (Figure 4a). The data shows multiple key points: (a) there is no 1-to-1 relationship between $PR_{AA}$ and $PR_{RR}$; (b) the largest $PR_{RR}$ events occur in cases in which the precipitating region (within 1000 km of the cyclone center) is relatively small; (c) and on the other hand, as $PR_{AA}$ increases, the lower limit of $PR_{RR}$ increases as well, that is, generating a large $PR_{AA}$ is not dependent on the area of the precipitation region alone. Thus, large $PR_{AA}$ depends both on precipitation occurring over a large region and the rain rates being at least moderate. On the other hand, $PR_{RR}$ tends to maximize in cases where the precipitation region is small.

Figure 4b shows the relative frequency of precipitation rates after sorting the grid cells based on the occurrence of convection. The data show that grid cells with convection have larger precipitation rates more frequently than nonconvective grid cells. The difference in the distribution is statistically significant, based on a Kolmogorov-Smirnov difference-of-distributions test at the 99th percentile. This is consistent with previous studies for tropical regions (Steiner et al., 1995). As further proof of this result, if we isolate the convective cells in which subgrid convective extent is 100%, the distribution has a statistically significant shift towards even larger probabilities of stronger precipitation.

Recall that convective contribution measures the role of convection relative to the total precipitation. $PR_{RR}$ has a weak but positive linear relationship with convective contribution (Figure 4c), signaling that if the intensity of precipitation in the raining regions is high, it is likely that there is a large contribution from convection. This analysis re-enforces the Figure 4b result.

Finally, Figure 4d shows the relationship between convective contribution and area-averaged total precipitation rates ($PR_{AA}$). For cyclones with large precipitation rates, there is not a lot of contribution from convection and the cyclones with the largest convective contribution tend to have small $PR_{AA}$ (Figure 4d). These results are consistent with results from model analysis (Booth et al., 2018; their figure 6). This implies that the total amount of precipitation generated by convection in ETCs with larger area-total precipitation rates is similar to that of an ETC with lower area-total precipitation rates. Note that this analysis of $PR_{AA}$ (i.e., Figure 4d) cannot be directly compared with the results in Figure 2b. This is because in Figure 2b, each separate cyclone track is sorted by precipitation life cycle. If a cyclone track is relatively dry compared with other cyclone tracks, it will still have its own maximum $PR_{AA}$ which will be placed in the $t = 0$ bin in Figure 2 b. Meanwhile, in Figure 4, all cyclones are sorted based on $PR_{AA}$, allowing the very heavy precipitating events to stand out.

No relationship is seen between the amount of convection and its latitude (not shown): ETCs at higher latitudes have similar contributions of convective activity to the total precipitation as ETCs at lower latitudes. However, there is a correlation between latitude and total precipitation (not shown): ETCs at higher latitudes have lower precipitation rates than ETCs at lower latitudes, likely due to less available water vapor (e.g., Booth, Naud, & Willison, 2018). Our analysis suggests that upright convection in ETCs is not dependent on total precipitation or latitude (and therefore available water vapor). This result may reflect the fact that multiple different processes other than convective activity, such as moisture convergence (e.g., Wong et al., 2018), affect the total precipitation amount.

## 4. Summary and Discussions

For the cyclones analyzed, the majority of convection occurs in the warm frontal and warm sector during initial stages of the ETC, and then later in the life cycle, the relative amount of convective precipitation near the cold front increases. However, upright convection does not occur preferentially at lower latitudes, and it is not confined to heavy precipitation regions. In fact, the cyclones generating the most precipitation within a 1,000-km radius of their centers do not have a large contribution from convection (i.e., Figure 4d), meaning that the existence of convection does not guarantee that an ETC will generate extreme precipitation totals. This suggests that the dynamics for generating convection during an ETC (occurring over the United States, east of the Rockies) are not driven by the same processes that control the overall precipitation of the cyclone.

Upright convection is scattered throughout the domain of the ETCs, occupies 1%–5% of the precipitating region of the ETC (on a 4-km grid) and contributes 1%–15% of the total precipitation. The largest contributions from convection occurred in summer. Time resolution inconsistencies in rainfall data and convection classifications used means that the amount of precipitation from convection may be slightly underestimated since precipitation rates in convection are often more intense than those in stratiform regions. The thresholding we use to identify convection may also impact on these numbers. However, small values for convective extent and contribution are consistent with the idea that most precipitation in ETCs is driven by isentropic ascent or slantwise convection. The spatial extent of the upright convection is comparable with the size of WCB regions (e.g., Schemm et al., 2013; Wernli & Davies, 1997) This is not to say that WCBs always involve upright convection, but it raises a new question regarding the dynamical impacts of the unique vertical profile of heating caused by upright convection on ETCs.

Relevant to climate models, our results can serve as a benchmark for model comparison. In terms of convective contribution to cyclone precipitation totals, our results are directly applicable. For convective extent, two keys steps must be taken: (a) when re-gridding our results to GCM resolution, the convective fraction information must be included, and (b) GCM output must include details regarding the subgrid assumptions made by the convection parameterization. As proof, consider: if we re-grid convective extent to a 60-km grid and label grids with *any* convective activity as convective, then cyclone convective extent is increased to

30%–40%. This is essentially what GCM output looks like now—convective precipitation is written to the output grid without including information on the fraction of the model grid occupied by parameterized convection.

As a reminder, this study only includes ETCs over land because it uses ground-based radar. However, the combined radar–radiometer product from the GPM Core Observatory mission (Grecu et al., 2016), which is part of the Global Precipitation Mission, includes a flag for convection. As the GPM dataset grows with time, there will be an opportunity to assess the role of convective activity for ETCs globally.

# References

Agel, L., Barlow, M., Colby, F., Binder, H., Catto, J. L., Hoell, A., & Cohen, J. (2019). Dynamical analysis of extreme precipitation in the US northeast based on large-scale meteorological patterns. *Climate Dynamics*, *52*(3-4), 1739–1760. https://doi.org/10.1007/s00382-018-4223-2

Baldwin, M. E., & Mitchell, K. E. (1998). Progress on the NCEP hourly multi-sensor U.S. precipitation analysis for operations and GCIP research. In *Preprints, 2nd Symposium on Integrated Observing Systems, 78th AMS Annual Meeting* (pp. 10–11).

Bauer, M., Tselioudis, G., & Rossow, W. B. (2016). A new climatology for investigating storm influences in and on the extratropics. *Journal of Applied Meteorology and Climatology*, *55*(5), 1287–1303. https://doi.org/10.1175/JAMC-D-15-0245.1

Booth, J. F., Naud, C. M., & Jeyaratnam, J. (2018). Extratropical cyclone precipitation life cycles: A satellite-based analysis. *Geophysical Research Letters*, *45*, 8647–8654. https://doi.org/10.1029/2018GL078977

Booth, J. F., Naud, C. M., & Willison, J. (2018). Evaluation of extratropical cyclone precipitation in the North Atlantic Basin: An analysis of ERA-Interim, WRF, and two CMIP5 models. *Journal of Climate*, *31*(6), 2345–2360. https://doi.org/10.1175/JCLI-D-17-0308.1

Boutle, I. A., Belcher, S. E., & Plant, R. S. (2011). Moisture transport in midlatitude cyclones. *Quarterly Journal of the Royal Meteorological Society*, *137*(655), 360–373. https://doi.org/10.1002/qj.783

Catto, J. L., Shaffrey, L. C., & Hodges, K. I. (2010). Can climate models capture the structure of extratropical cyclones? *Journal of Climate*, *23*(7), 1621–1635. https://doi.org/10.1175/2009JCLI3318.1

Colle, B. A., Booth, J. F., & Chang, E. K. M. (2015). A review of historical and future changes of extratropical cyclones and associated impacts along the US East Coast. *Current Climate Change Reports*, *1*(3), 125–143. https://doi.org/10.1007/s40641-015-0013-7

Crespo, J. A., & Posselt, D. J. (2016). A-train-based case study of stratiform–convective transition within a warm conveyor belt. *Monthly Weather Review*, *144*(6), 2069–2084. https://doi.org/10.1175/MWR-D-15-0435.1

Elsaesser, G. S., Del Genio, A. D., Jiang, J. H., & van Lier-Walqui, M. (2017). An improved convective ice parameterization for the NASA GISS global climate model and impacts on cloud ice simulation. *Journal of Climate*, *30*(1), 317–336. https://doi.org/10.1175/JCLI-D-16-0346.1

Feng, Z., Leung, L. R., Houze, R. A. Jr., Hagos, S., Hardin, J., Yang, Q., et al. (2018). Structure and evolution of mesoscale convective systems: Sensitivity to cloud microphysics in convection-permitting simulations over the United States. *Journal of Advances in Modeling Earth Systems*, *10*(7), 1470–1494. https://doi.org/10.1029/2018MS001305

Flaounas, E., Lagouvardos, K., Kotroni, V., Claud, C., Delanoë, J., Flamant, C., et al. (2016). Processes leading to heavy precipitation associated with two Mediterranean cyclones observed during the HyMeX SOP1. *Quarterly Journal of the Royal Meteorological Society*, *142*, 275–286. https://doi.org/10.1002/qj.2618

Gelaro, R., McCarty, W., Suárez, M. J., Todling, R., Molod, A., Takacs, L., et al. (2017). The modern-era retrospective analysis for research and applications, Version 2 (MERRA-2). *Journal of Climate*, *30*(14), 5419–5454. https://doi.org/10.1175/JCLI-D-16-0758.1

Global Modeling and Assimilation Office (GMAO) (2015). MERRA-2 tavg1_2d_slv_Nx: 2d,1-hourly, time-averaged, single-level, assimilation, single-level diagnostics V5.12.4, Greenbelt, MD, USA, Goddard Earth Sciences Data and Information Services Center (GES DISC). https://doi.org/10.5067/VJAFPLI1CSIV

Grecu, M., Olson, W. S., Munchak, S. J., Ringerud, S., Liao, L., Haddad, Z., et al. (2016). The GPM Combined Algorithm. *Journal of Atmospheric and Oceanic Technology*, *33*(10), 2225–2245. https://doi.org/10.1175/JTECH-D-16-0019.1

Hawcroft, M., Dacre, H., Forbes, R., Hodges, K., Shaffrey, L., & Stein, T. (2017). Using satellite and reanalysis data to evaluate the representation of latent heating in extratropical cyclones in a climate model. *Climate Dynamics*, *48*(7–8), 2255–2278. https://doi.org/10.1007/s00382-016-3204-6

Hawcroft, M. K., Shaffrey, L. C., Hodges, K. I., & Dacre, H. F. (2012). How much Northern Hemisphere precipitation is associated with extratropical cyclones? *Geophysical Research Letters*, *39*, L24809. https://doi.org/10.1029/2012GL053866

Hewson, T. D. (1998). Objective fronts. *Meteorological Applications*, *5*(1), 37–65. https://doi.org/10.1017/S1350482798000553

Hobbs, P. V. (1978). Organization and structure of clouds and precipitation on the mesoscale and microscale in cyclonic storms. *Reviews of Geophysics*, *16*(4), 741–755. https://doi.org/10.1029/RG016i004p00741

Homeyer, C. R., & Bowman, K. P. (2017). Algorithm description document for version 3.1 of the three-dimensional Gridded NEXRAD WSR-88D (GridRad) dataset. Tech. rep., available online at http://gridrad.org

Homeyer, C. R., Schumacher, C., & Hopper, L. J. (2014). Assessing the applicability of the tropical convective–stratiform paradigm in the extratropics using radar divergence profiles. *Journal of Climate*, *27*(17), 6673–6686. https://doi.org/10.1175/JCLI-D-13-00561.1

Houze, R. A. Jr. (2014). Cloud Dynamics (2 edition). Amsterdam, New York: Academic Press.

Houze, R. A., Hobbs, P. V., Biswas, K. R., & Davis, W. M. (1976). Mesoscale rainbands in extratropical cyclones. *Monthly Weather Review*, *104*(7), 868–878. https://doi.org/10.1175/1520-0493(1976)104<0868:MRIEC>2.0.CO;2

Lin, Y., & Mitchell, K. E. (2005). The NCEP Stage II/IV hourly precipitation analyses: Development and applications. In *Preprints, 19th Conf. on Hydrology, American Meteorological Society, San Diego, CA, 9-13 January 2005, Paper 1.2*. Retrieved from http://www.emc.ncep.noaa.gov/mmb/ylin/pcpanl

Naud, C. M., Booth, J. F., & del Genio, A. D. (2016). The relationship between boundary layer stability and cloud cover in the post-cold-frontal region. *Journal of Climate*, *29*(22), 8129–8149. https://doi.org/10.1175/JCLI-D-15-0700.1

Naud, C. M., del Genio, A. D., Bauer, M., Kovari, W. (2010). Cloud vertical distribution across warm and cold fronts in CloudSat–CALIPSO data and a general circulation model. *Journal of Climate*, *23*(12), 3397–3415. https://doi.org/10.1175/2010JCLI3282.1

Oertel, A., Boettcher, M., Joos, H., Sprenger, M., Konow, H., Hagen, M., & Wernli, H. (2019). Convective activity in an extratropical cyclone and its warm conveyor belt—A case-study combining observations and a convection-permitting model simulation. *Quarterly Journal of the Royal Meteorological Society*, *145*, 1406–1426. https://doi.org/10.1002/qj.3500

Pfahl, S., & Wernli, H. (2012). Quantifying the relevance of cyclones for precipitation extremes. *Journal of Climate*, *25*(19), 6770–6780. https://doi.org/10.1175/JCLI-D-11-00705.1

Reed, R. J., Grell, G. A., & Kuo, Y.-H. (1993). The ERICA IOP 5 Storm. Part II: Sensitivity tests and further diagnosis based on model output. *Monthly Weather Review*, *121*(6), 1595–1612. https://doi.org/10.1175/1520-0493(1993)121<1595:TEISPI>2.0.CO;2

Schemm, S., Wernli, H., & Papritz, L. (2013). Warm conveyor belts in idealized moist baroclinic wave simulations*. *Journal of the Atmospheric Sciences*, *70*(2), 627–652. https://doi.org/10.1175/JAS-D-12-0147.1

Simmonds, I., Keay, K., & Tristram Bye, J. A. (2012). Identification and climatology of southern hemisphere mobile fronts in a modern reanalysis. *Journal of Climate*, *25*(6), 1945–1962. https://doi.org/10.1175/JCLI-D-11-00100.1

Starzec, M., Homeyer, C. R., & Mullendore, G. L. (2017). Storm labeling in three dimensions (SL3D): A volumetric radar echo and dual-polarization updraft classification algorithm. *Monthly Weather Review*, *145*, 1127–1145. https://doi.org/10.1175/MWR-D-16-0089.1

Steiner, M., Houze, R. A., & Yuter, S. E. (1995). Climatological characterization of three-dimensional storm structure from operational radar and rain gauge data. *Journal of Applied Meteorology*, *34*(9), 1978–2007. https://doi.org/10.1175/1520-0450(1995)034<1978:CCOTDS>2.0.CO;2

Tierney, G., Posselt, D. J., & Booth, J. F. (2018). An examination of extratropical cyclone response to changes in baroclinicity and temperature in an idealized environment. *Climate Dynamics*, *51*(9-10), 3829–3846. https://doi.org/10.1007/s00382-018-4115-5

Wernli, B. H., & Davies, H. C. (1997). A Lagrangian-based analysis of extratropical cyclones. I: The method and some applications. *Quarterly Journal of the Royal Meteorological Society*, *123*, 467–489. https://doi.org/10.1002/qj.49712353811

Wong, S., Naud, C. M., Kahn, B. H., Wu, L., & Fetzer, E. J. (2018). Coupling of precipitation and cloud structures in oceanic extratropical cyclones to large-scale moisture flux convergence. *Journal of Climate*, *31*, 9565–9584. https://doi.org/10.1175/JCLI-D-18-0115.1

Zhao, M., Golaz, J.-C., Held, I. M., Guo, H., Balaji, V., Benson, R., et al. (2018). The GFDL global atmosphere and land model AM4.0/LM4.0: 2. Model description, sensitivity studies, and tuning strategies. *Journal of Advances in Modeling Earth Systems*, *10*(3), 735–769. https://doi.org/10.1002/2017MS001209

## Erratum

In the originally published version of this article, the supporting information was omitted. This error has since been corrected, and the present version may be considered the authoritative version of record.